Acoustic emission monitoring during gas permeation: a new operando diagnostic tool for porous membranes

Micka Bah, Etoungh Manga, Hugues Blasco, Philippe Da Costa, Martin Drobek, André Ayral, Gilles Despaux, Benoit Coasne, Emmanuel Le Clezio, Anne Julbe

Acoustic emission monitoring during gas permeation: a new *operando* diagnostic tool for porous membranes

Micka Bah[1,2], Etoungh D. Manga[1,2], Hugues Blasco[1], Philippe da Costa[1], Martin Drobek[1], André Ayral[1], Gilles Despaux[2], Benoit Coasne[3,*], Emmanuel Le Clezio[2,*] Anne Julbe[1,*]

[1] Institut Européen des Membranes (UMR 5635 CNRS, ENSCM, UM), Université de Montpellier, 34095 Montpellier, France
[2] Institut d'Electronique et des Systèmes (UMR 5214 CNRS, UM), Université de Montpellier, 34095 Montpellier, France
[3] Univ. Grenoble Alpes, CNRS, LIPhy, 38000 Grenoble, France

*Corresponding authors:
benoit.coasne@univ-grenoble-alpes.fr,
emmanuel.le-clezio@umontpellier.fr,
anne.julbe@umontpellier.fr

Abstract:

In the area of membrane separations the development of powerful *on-line* diagnostic tools allowing the reliability insurance of both membranes and associated processes becomes a major concern. In this context, Acoustic Emission (AE) appears as a potentially attractive method to ensure *i)* quality control for membrane production lines and *ii) on-line* monitoring of their evolution when implemented in integrated industrial systems requiring high level of safety/security. In this work, simultaneous gas permeation measurements and acoustic emission technique have been coupled in order to characterize series of porous membranes operating under various conditions. AE events resulting from different gas transport mechanisms through porous membranes series have been identified and classified thanks to a statistical post-treatment of the recorded acoustic signals. A close relationship between AE signal characteristics, physicochemical properties of the porous membranes and associated gas transport mechanisms was established. These promising results constitute a key step in the development of an innovative tool for non-invasive *on-line* diagnosis dedicated to the characterization and control of porous ceramic membranes.

Keywords: Porous ceramic membranes, Acoustic emission, Gas permeation, Transport mechanism, Characterization, *On-line* diagnostic tool.

1. Introduction

Membrane separation processes are efficient and economically attractive technologies used in many areas of everyday life such as water treatment, agri-business/food-processing, health-related applications, environment protection, systems associated with energy production, etc. [1-5]. Moreover, many innovative strategies are being considered to implement membrane materials to the full spectrum of key separation technologies such as greenhouse gases abatement or alkene/alkane separations [6]. A great deal of effort is also devoted to membrane processes carried out under severe conditions such as high pressures or chemically harsh environments in catalytic reactors or other integrated systems [7-9]. In the area of porous membranes, the transport properties and separation performance are directly related to their pore structure and surface characteristics. Both the bulk and surface physico-chemical properties (charge, hydrophilic/hydrophobic nature, chemical composition…) play an important role in transport mechanisms and govern, to some extent, the interactions between the molecules and the membrane surface. In addition to these physicochemical properties, the pore structure parameters (including defects, if any) are of the utmost importance due to their impact on membrane performance. These parameters have to be measured and controlled, more or less drastically, depending of the target application. In this context, in parallel to the development of sophisticated and defect-free membranes for highly efficient gas separation operations [10-11], *on-line* quality control systems are urgently needed in order to address all safety constraints associated with the transfer of these new technologies from lab-scale to industry. Owing to the close link between the membranes microstructure and their performance [12-14], many characterization techniques probing their transport and morphological properties (such as pore size, surface chemistry and pore connectivity but also active pathways and defects) are available: *i)* stereological (microscopy, tomography, etc.), *ii)* static intrusive (gas adsorption, intrusion porosimetry, etc.), *iii)* static non-intrusive

(ultrasounds, positron annihilation, etc.), and *iv)* dynamic methods (permeation, chromatography, etc.) methods. Static intrusive methods are often used as a first analysis tool of the membrane pore structure, while non-intrusive methods are suitable for the detection of non-interconnected pores and also for *operando* membrane characterization. Dynamic techniques provide insight into the complex link between the membrane microstructure and transport behavior. These methods are not limited regarding the small quantity of membrane material and are sensitive to the active pathways through the pore structure, including defects. However, as far as continuous characterization during operation is concerned, only non-intrusive techniques can be considered such as ultrasonic testing, radiography, X-ray tomography, or acoustic emission (AE).

Among the non-invasive tools listed above, ultrasonic techniques have been used for real-time monitoring of polymeric membranes formation [15] and membrane fouling (*e.g.* during filtration of solutions containing calcium sulphate [16] or animal proteins [17]). Ultrasonic reflectometry was also combined with capacitive microsensors [18] that can respond to solute concentration variation for real-time monitoring of the concentration polarization until the fouling of the filtering membrane. On the other hand, these techniques do not allow probing the level of membrane damage or the integrity of the membrane process. In contrast, AE is a unique method enabling continuous *on-line* monitoring and control of both the membrane material and the separation process [19]. Indeed, AE can be defined as "*the class of phenomena in which transient elastic waves are generated by the rapid release of energy from a localized source(s) within a material"* [20]. When an energy release occurs in a material, a part of this energy (often small) can be emitted as a transient, elastic stress or strain wave (typically in the range 50 kHz – 1 MHz). AE can be either continuous (waveform) or discontinuous (bursts). Continuous emission means that the signal amplitude is slightly larger than the background noise; AE events occur closely in time and form a single waveform. A

burst emission leads to signal amplitudes much larger than the background noise; AE events are of a short duration and are well separated in time.

As far as ceramic-based materials are concerned, the rate and intensity of AE can be used to detect the initiation and propagation of cracks and delamination. Hence, AE testing is a useful technique to predict static and fatigue failure in industrial structures (e.g. during tensile testing, cyclic mechanical loading, tension-tension fatigue loading). Despite satisfactory results obtained in various material areas [21-24], AE has not yet been explored to monitor the behavior of porous membranes during fluid transport and its application to granular media mainly concerns the geology of rocks [25-26].

Indeed, owing to its low cost, high sensitivity and non-invasive nature, AE is perfectly suited for application in membrane technologies as it might allow quality control of membrane top-layers on separation lines. Finally, this sensitive and non-invasive technique also provides an efficient tool for *on-line* monitoring of industrial membrane processes (by providing necessary safety for large-scale devices implementing membrane modules in industrial systems). In particular, the coupling of a non-intrusive characterization method such as AE with a dynamic method (permeation) is an attractive approach to (1) probe permeation modes, (2) evaluate the membrane top-layer integrity, and (3) detect defect formation under static conditions or during transition regimes (thermal or pressure cycling, change in fluid composition, etc.).

A very first step towards the development of an *operando* characterization of porous membranes by means of focused acoustic microscopy combined with atom-scale simulation has been published by the authors few years ago [27]. It was shown that simple molecular simulations of gas adsorption can be used to predict the mechanical and acoustic behavior of a zeolite membrane layer depending on the applied gas pressure. In the present work, we investigate the coupling of acoustic emission and gas transport measurements to show that gas

permeation through porous membranes has a clear acoustic footprint. Different single gases (He, N_2, and CO_2) and porous ceramic membranes series (pore sizes from ~ 0.55 nm to 10 μm) were considered. Based on a statistical post-treatment of the recorded single waveforms, we demonstrated a close relationship between AE signals, gas properties, gas transport mechanisms and the physicochemical properties of the porous membranes. We showed that AE at the resonance frequency of the membrane support and its harmonics is triggered by the viscous flow. Thanks to a model relying on the coupling between the membrane hydrodynamic mode and the support acoustic mode, we explained the frequency at which AE is observed, the effect of gas molecule, and the minimum pressure/velocity required to induce the phenomenon.

2. Experimental details

2. 1. Porous ceramic membranes

The tested membranes consist of a commercial single channel ceramic tube with the porous top-layer on its inner surface (length L_{tube} ~ 15 cm and inner/outer diameters $\varnothing_{in}$ ~ 0.6-0.7 cm and $\varnothing_{out}$ ~ 1 cm). More precisely, the wall of the ceramic tube features the multilayer, asymmetric and multiscale structure depicted in **Figure 1**. The external layer (outer surface) of the ceramic tube is macroporous. The interlayers are also macroporous but with smaller pore sizes. The top-layer (which can be macro-, meso- or microporous [28] is deposited at the inner surface of the ceramic tube, *i.e.* on-top of the last macroporous layer acting as a support. Such a classical asymmetric structure allows minimizing the top-layer thickness and its associated transport resistance while ensuring high mechanical stability of the whole membrane system. The ceramic tube extremities (inner and outer surfaces) were sealed with a commercial enamel (annealed at 950°C) to avoid any direct gas transport through the support cross-section. Only a small central region, with a length L_m ~ 0.8-1.5 cm, was available for gas transport

Table 1 displays some key properties of the different membrane samples tested in this work. The ceramic supports and top-layers have different compositions (alumina, silica, titania) and pore diameters (D ~ 0.55 nm, 8 nm, 55 nm, 100 nm, 800 nm, and 10 μm). The microporous MFI (silicalite-1) zeolite top-layer exhibits pores with a mean diameter D ~ 0.55 nm. Zeolites were grown on a Pall-Exekia support (α-Al_2O_3 – 200 nm - already enameled) according to the protocol described by Drobek and co-workers [29]. The γ-Al_2O_3 top-layer is mesoporous with its initial pore size D ~ 5 nm, which increased to ~ 8 nm after the enameling treatment at 950°C. The Al_2O_3/TiO_2 top-layer is meso/macroporous with its initial pore size D ~ 50 nm, which increased to ~ 55 nm after the enameling treatment. The three other samples correspond to macroporous α-Al_2O_3 top-layers with pore sizes D ~ 100 nm, 800 nm, and 10 μm.

2. 2. Acoustic emission

Continuous acoustic emission (CAE) was investigated for the different membranes during single gas permeation operation, using the experimental set-up shown in **Figure 2**. The ceramic membranes were installed in a specific permeation cell designed to optimize CAE detection. The gas was injected at a given pressure and temperature ~21°C into the permeation cell in dead-end configuration and the gas flux through the permeable region was measured by bubble flowmeter at atmospheric pressure. CAE upon gas permeation was detected thanks to an ultrasonic transducer placed on an aluminum disc in contact with the ceramic tube (enameled region). A coupling gel (Eurosonic Group) was used for efficient airless and flawless contact between the transducer and the ceramic tube. The ultrasonic transducer was a R15-α, exhibiting a resonant frequency of 75 kHz and an operating frequency range of [50-400] kHz. The transducer was 19 mm in diameter and 22.4 mm in height. The entire system (transducer and gas permeation cell) was placed in a sound insulation box to avoid any external parasitic noise influencing the measurements. For CAE

displaying and recording, the transducer was connected through a 40 dB-gain preamplifier (EPA 1220A) to the Mistras-2003 acquisition system (Euro Physical Acoustics S.A.). The plug-in filter had a bandwidth in the range 1 kHz - 1 MHz. Before and after each measurement, the transducer coupling was checked with the Hsu-Nielsen calibration source [30].

The waveform streaming measurement approach was applied to the permeating porous membranes thanks to a PCI-2 acoustic emission system provided by Mistras Group Inc. The wave streaming data were post-treated using a LabVIEW software interface. Fourier transform treatment was performed at periodic temporal intervals, allowing the mapping of the signal amplitude versus both frequency and time (or pressure).

2. 3. Laser vibrometry

The AE analysis (measuring mechanical vibrations from all parts of the measurement cell) was completed by local measurements using laser vibrometry. The normal displacement field was measured at the outer surface of the tube using a POLYTEC OFV-534 compact laser vibrometer. The measurement principle relies on the modulation of the laser beam when it is reflected on the moving surface; the normal displacement speed of the surface generates a Doppler frequency modulation of the emitted laser light. The demodulator used is VD02, a decoder usable for frequencies less than 1.5 MHz. Comparison between the reflected signal and a reference signal emitted by the laser allows measuring the vibration rate by the laser detector. A voltage proportional to the normal component of the surface velocity is then delivered. The sensitivity is 5 $mm.s^{-1}.V^{-1}$ at a measurement frequency of 350 kHz. The measured velocity at the surface of the sample is of the order of $mm.s^{-1}$. After integration of the measured velocity, the output voltage of the detection laser is proportional to the amplitude of the displacement component. A reflective strip adhered along the measurement

axis was used to ensure a good surface reflectivity and therefore a satisfactory signal-to-noise ratio.

2. 4. Single gas permeation

The acoustic footprint of gas transport through membrane series was investigated at room temperature for three selected single gases: He, N_2 and CO_2. The main physical properties of these gases (molecular weight, mass density, dynamic viscosity, and kinetic diameter) are reported in **Table 2**. These properties impacting gas diffusivity, flow velocity/type, permeance values, and sound velocity, are expected to impact on the membranes acoustic signatures.

In order to detect possible acoustic emission during single gas permeation with He, N_2 or CO_2, the transmembrane pressure across the tube was varied from 0 to 5 bars for a total cycle time of ~ 220 s. First, the transmembrane pressure ΔP was set to 0 bar during 20 s to record the streaming signal that serves as reference spectrum for other pressures. The ΔP value was then increased in a stepwise fashion from 0 to 1 bar thanks to a micrometric valve with a rise time of 10 s and then stabilized for at least 30 s (dwell time) while recording the waveform streaming signal. This protocol was repeated at transmembrane pressures ΔP = 2, 3, 4, and 5 bars and the waveform streaming signals were continuously recorded during 220 s. Before any measurement with a new gas, the membrane placed in the permeation cell was submitted to a 20 min outgassing treatment under vacuum to avoid any influence of the previous gas on the measured waveform streaming signal.

3. Results and discussion

3. 1. Single gas membrane permeances and gas transport regimes

In all permeation experiments, the membranes did not yield any discrete acoustic emission (DAE). While DAE is observed when gas leakage or membrane cracking occurs, the present

paper focuses on establishing the direct link between CAE and gas permeation through porous membranes. At first, the nature of the gas flow has been examined. Reynolds numbers have been estimated for the top-layers; $Re = \rho v D/\eta$ where ρ is the gas density, v the measured flow velocity, η the gas dynamic viscosity and D the pore mean diameter in the top-layer [31]. Considering the data shown in **Tables 1** and **2**, we found that $Re < 10^{-2}$ for all the measured membranes, gases, and pressure gradients under study – with the exception of the membrane with $D \sim 10$ µm which is too permeable and yields flows out of the accuracy range. Reynolds numbers (Re) for N_2 and CO_2 are about an order of magnitude larger than for He. The calculated Re values, ($Re << 1$), show that the flow through the different membranes can be assumed to be non-turbulent ($Re \sim 2000$ corresponds to the transition between laminar and turbulent flows).

The permeance Π, defined as the transport coefficient relating the gas flow to the transmembrane pressure ($J = -\Pi \Delta P$), was first estimated for N_2, He, and CO_2 at 21°C. **Figure 3** shows the evolution of N_2 permeance as a function of the applied mean pressure P_m for the different membranes. Note that these data were plotted as a function of $P_m = \Delta P/2 + P_{atm}$ where ΔP is the transmembrane pressure and P_{atm} the atmospheric pressure. For a given gas, the permeance Π increases with both the mean gas pressure P_m and the membrane mean pore size D, with Π values in the range $10^{-6} - 10^{-4}$ mol.Pa^{-1}.s^{-1}.m^{-2} (for $P_m \sim 1.2$ - 2.3 bar). At a given pressure, Π values for the membranes with top-layer pore sizes D = 0.55 nm, 8 nm, 55 nm, and 100 nm are respectively ~25, 3, 2, and 1.5 times smaller than the permeance for D = 800 nm.

Figure 3 shows that the membrane permeance increases linearly with the mean gas pressure, $\Pi = aP_m + b$. For non-turbulent flows, several gas transport mechanisms such as viscous flow,

Knudsen diffusion, surface diffusion, multilayer diffusion, capillary condensation, and configurational diffusion contribute to the total gas permeance Π of porous membranes [32-34]. Among these different contributions, surface/multilayer diffusion and capillary condensation can be neglected when considering either permeation of non-condensable gases such as He at room temperature or gas transport through macroporous membranes (because of negligible adsorption for the former and negligible specific surface area for the latter). The total gas permeance Π can therefore be expressed as $\Pi = \Pi_v + \Pi_K$ where Π_v is pressure dependent and corresponds to the viscous/configurational diffusion contribution while Π_K is pressure independent and corresponds to the Knudsen diffusion contribution. Regarding Π_v, it is known that, upon decreasing the pore size, there is a crossover between viscous flow (large pores) and molecular diffusion (small pores). Such a transition has been shown to arise from the breakdown of the viscous flow assumption in very small nanopores where there is no timescale separation between microscopic relaxation and hydrodynamics [34]. Yet, as shown in Ref. [35,36], even in very small pores, a Darcy-like description still holds provided the permeance is estimated from the collective diffusivity. As a result, for the sake of simplicity, we refer for all top-layer pore sizes to the viscous contribution Π_v but it should be kept in mind that it could correspond to different underlying pressure-dependent mechanisms. A detailed investigation of the relative contributions of all types of pressure-dependent and non-pressure dependent transport mechanisms will be considered in future works, with other types of gases and membrane materials. This will be particularly relevant for the microporous membranes in which sorption phenomena and defect contributions to gas transport can be huge.

The pressure-dependent contribution Π_v can be estimated from the corresponding flow, $J_v = -\Pi_v \Delta P$ where ΔP is the transmembrane pressure. In the stationary regime, the drag force corresponding to the applied pressure, $F_d = \pi r^2 \Delta P$ (r is the pore size), counterbalances the viscous force, $F_v = -8\pi\eta\tau L_m v$ (η and v are the gas dynamic viscosity and flow velocity while

τ is the tortuosity that accounts for morphological and topological effects along the fluid path within the top-layer, and L_m is the top-layer active length). If we compare these two forces, we arrive at Darcy's equation that relates the flow velocity to the transmembrane pressure through the tortuosity-corrected permeability $k = r^2/8\tau$; i.e. $v = -k/\eta\ \Delta P/L_m$. By comparing the two expressions for the viscous flow, $J_v = -\Pi_v \Delta P$ and $J_v = \langle\rho\rangle v$ where $\langle\rho\rangle$ is the average gas density within the top-layer, we obtain that $\Pi_v = \phi P_m/8\eta k_B T L_m$. In this equation, we used the ideal gas equation and the top-layer porosity ϕ to estimate $\langle\rho\rangle = \phi P_m/k_B T$ from the average applied pressure $P_m = \Delta P/2 + P_{atm.}$ (ΔP is the transmembrane pressure and P_{atm} is the atmospheric pressure). Similarly, the Knudsen contribution can be estimated from the corresponding flow, $J_k = -\Pi_k \Delta P$. In the Knudsen regime, the flux writes $J_k = -w\ v_T\ \Delta\rho/\tau$, where $v_T = \sqrt{8k_B T/\pi m}$ is the average thermal velocity, $w = 2r/3L_m$ (for $r << L_m$) is the probability that a molecule passes through a pore, τ is the top-layer tortuosity, and $\Delta\rho$ is the gas density difference across the pore length. $\Delta\rho = \phi\Delta P/k_B T$ can be estimated using the ideal gas equation (again, the porosity ϕ is used to correct for the volume inaccessible to the gas inside the membrane). Π_k can be obtained by comparing $J_k = -\Pi_k \Delta P$ and $J_k = -w\ v_T\ \Delta\rho/\tau$; $\Pi_k = 2r\phi/3L_m\tau \times \sqrt{8/\pi m k_B T}$. Considering the different contributions above, the total permeance becomes:

$$\Pi = \frac{\phi k P_m}{\eta k_B T L_m} + \frac{2r\phi}{3L_m\tau}\sqrt{\frac{8}{\pi m k_B T}} \qquad (1)$$

The parameters $a = \frac{\phi k}{\eta k_B T L_m}$ and $b = \frac{2r\phi}{3L_m\tau}\sqrt{\frac{8}{\pi m k_B T}}$, which were determined by linear regression for each membrane, are reported in **Supplementary Table S1** (the linear fits are shown as dashed lines in **Figure 3**). These data show that the viscous contribution, estimated at a reference pressure of P_m = 1.25 bar, is about 60, 40, 30, 20, and 10% of the total flow for

the membrane with top-layer pore sizes D = 800 nm, 100 nm, 55 nm, 8 nm, and 0.55 nm, respectively. Such contributions are consistent with Knudsen numbers Kn defined as the ratio of the mean free path λ to the pore size D, Kn = λ/D with $\lambda = \frac{\eta}{P_m}\sqrt{\frac{\pi k_B T}{2m}}$. For P_m = 1.25 bar and T = 21°C, λ ~ 53 nm, 155 nm, and 35 nm for N_2, He, and CO_2 respectively, leading to Kn in the range [10^{-3} – 10^{2}].

The insert of **Figure 3** shows the He, N_2, and CO_2 permeances as a function of the mean pressure P_m for the membrane with a top-layer pore size D ~ 55 nm. The data for He and CO_2 also show that the permeance increases linearly with P_m, in agreement with the permeance model discussed above leading to Eq. (1). The parameters $a = \frac{\phi k}{\eta k_B T L_m}$ and $b = \frac{2r\phi}{3L_m\tau}\sqrt{\frac{8}{\pi m k_B T}}$ determined by linear regression for each gas are shown in **Supplementary Table S2** (with the corresponding fits shown as dashed lines in the insert of **Figure 3**). The viscous contribution at a reference pressure of P_m = 1.25 bar is about 46% for He, 31% for N_2 and 32% for CO_2 for the membrane with a top-layer pore size D = 55 nm. As expected, considering the mass of the different gases (see **Table 2**), $b \sim 1/\sqrt{m}$ and $b_{He} > b_{N2} > b_{CO2}$. In contrast, while $a \sim \eta^{-1}$ should be the smallest for He and the largest for CO_2, we observe $a_{He} > a_{N2} \sim a_{CO2}$. This result shows that adsorption at the pore surface in the top-layer is not completely negligible so that the viscous flow is affected (decreased because of molecular residence time at the surface). This interpretation is consistent with the fact that CO_2 adsorption is expected to be the most important owing to its strong quadrupole, followed by N_2 adsorption also possessing a non-negligible quadrupole that interacts with the oxide surface of the top-layers. In contrast, He can be reasonably assumed to be fully non-adsorbable at room temperature so that its adsorption-free viscous contribution is the largest.

In particular, slippage could arise owing to the very weak interaction between He and the oxide surface.

3.2. Acoustic signature of porous membranes upon gas permeation.

Figure 4 shows contour plots of the CAE amplitude as a function of time t and frequency f for the different membranes upon N_2 gas permeation. As shown in the data for the membrane with D = 10 μm (porous support alone), the applied transmembrane pressure was varied from 0 to 5 bars in a stepwise fashion (so that the time axis can be converted into a pressure axis - see the methods section for details). Except the membrane with the smallest top-layer pore size (D ~ 0.55 nm), all other membranes yield intense spectral signatures provided that the transmembrane pressure is large enough. The transmembrane pressure threshold, ΔP_c, above which CAE is observed decreases with increasing the pore size (in fact, it is believed that CAE would be observed for the smallest pore size if transmembrane pressures larger than 5 bar were applied). Upon increasing the transmembrane pressure above ΔP_c, the CAE signal amplitudes increase and additional frequencies appear in the acoustic spectrum; only acoustic modes in the frequency range ~10 kHz are observed for ΔP slightly above ΔP_c but additional acoustic modes are observed at well-defined frequencies in the range ~2 – 250 kHz as ΔP is further increased. Interestingly, the frequencies observed in these acoustic spectra do not depend on the membrane so that it can safely be assumed that they correspond to acoustic modes of the enameled ceramic support. However, as discussed in detail below, such acoustic modes are activated for minimum transmembrane pressures that depend on the top-layer pore size.

To assess the modes observed in the acoustic spectra, we show in **Figure 5a** the acoustic amplitude A_f as a function of frequency f for the membrane with D ~ 10 μm measured at different transmembrane pressures up to ΔP = 5 bars. We emphasize that similar spectra were

observed – although with different pressure thresholds – for the other membranes. The data in **Figure 5a** correspond to the stationary regime *i.e.* beyond the transient regime observed after increasing in a stepwise manner the transmembrane pressure ΔP. As expected from **Figure 4**, despite non-negligible noise, while no acoustic mode is observed when no gas flows through the membrane (ΔP = 0 bar), intense peaks appear upon increasing the transmembrane pressure ΔP. Only peaks in the range 10-15 kHz are observed for ΔP = 1 bar although other peaks appear when the pressure is increased above ΔP = 2 bar: a small peak at ~ 2 kHz, two peaks centered at ~ 23 kHz, and several peaks in the range 40-45 kHz.

The fact that the amplitude of the acoustic peaks increases with pressure raises the question of their activation: *do they become active at a specific i.e. threshold pressure (gas flow-induced activation) or are they already active at very low pressures but too weak to be measured (no gas flow-induced activation)?* Special attention must be paid when addressing this question, especially considering the following properties of the acoustic sensor (a disc with a diameter at least 10 times larger than its thickness to distinguish its *radial* from *thickness* modes – see Supplementary **Figure S1** for the frequency bandwidths corresponding to the different sensing modes). First, the acoustic sensor only detects vibrations with frequencies within its operating bandwidths: [~2 – 50 kHz] for its *radial* mode and [50 – 250 kHz] for its *thickness* mode. Second, the sensor sensitivity is not a monotonous/constant function of the vibration frequency *f* with an optimal detection window that is thought to be in the range from 10 to 20 kHz. As a result, some acoustic modes corresponding to high harmonic orders are probably not detected at all or with a very weak signal. Third, due to the specific boundary conditions inherent to our experimental setup (the tubular support is not free to vibrate as it is attached to the permeation cell), extinction rules apply.

To determine the nature (activated *versus* non-activated) of the acoustic modes, we plotted in **Figures 5b** and **5c** the amplitude of the acoustic signal corresponding to the acoustic

frequency f = 13 kHz and the cumulated acoustic amplitude in the range [146-190 kHz] as a function of the transmembrane pressure gradient $\nabla P = \Delta P/t$ (where t is the top-layer thickness) for N_2 flowing through the membranes. While the acoustic amplitude in the low frequency range corresponds to the intense peak around $f \sim 13$ kHz, the amplitude in the high frequency range is integrated over the range [146 – 190 kHz] to amplify their pressure dependence (in this frequency range, signal amplitudes are small yet non-negligible). Both the signals in the low and high frequency ranges show that CAE is only observed above a minimum pressure gradient ∇P_c which depends on the top-layer pore size. Indeed, the same data plotted in a log scale in the inserts **Figures 5b** and **5c** show that the acoustic amplitude is $A \sim 0$ for $\nabla P < \nabla P_c$ and then scales as $A \sim \ln \nabla P$ for $\nabla P < \nabla P_c$. This result provides evidence that acoustic modes are activated when a minimum pressure gradient, which depends on the top-layer pore size, is reached (note that, for non-activated modes, we should observe $A \sim \nabla P$ with no threshold effect). Considering that Knudsen permeance does not depend on the transmembrane pressure ΔP (see Eq. (1)), the existence of a minimum pressure gradient to induce CAE suggests that acoustic emission is driven by the viscous flow contribution (which depends on ΔP). This idea is supported by the fact that the viscous contribution at ∇P_c represents 46, 40, 42 and 60% of the total N_2 flow for pores sizes $D \sim 8$ nm, 55 nm, 100 nm and 800 nm, respectively.

The mechanisms behind the different acoustic modes were identified by plotting in **Figure 6a** the acoustic data corresponding to the membrane with the top-layer pore size $D \sim 100$ nm at a transmembrane pressure $\Delta P = 4$ bar (data at a high pressure were selected to make sure all acoustic peaks are observed). While this specific membrane was selected for a deeper investigation, we emphasize that very similar acoustic responses were observed for the other membranes (provided ΔP is above the corresponding threshold). We also investigated in the frequency range [0-40 kHz] the vibration modes for the same system using laser vibrometry

[37, 38] (**Figure 6b**). Due to this *local* technique (see experimental section -§2.3- for details), the vibration modes corresponding to the different components of our combined acoustic/permeation experiments could be probed: (1) gas entrance from the source/gas feed, (2) gas exit towards the flowmeter, (3) aluminum disc attached to the ceramic support, and (4) the ceramic support itself on which other layers are deposited. Owing to their different resolutions/sensitivities, responses (*i.e.* acoustic *versus* optical) including possible frequency shifts, extinction rules including harmonics selectivity, the comparison between acoustic and optical techniques applied to determine the vibration modes is far from trivial. Yet, the acoustic and optical spectra in **Figures 6a** and **6b** show some interesting similarities that shed light on the fundamental mechanisms behind acoustic modes observed for the different membranes.

The acoustic peak observed at about 2-3 kHz is also observed when applying laser vibrometry to the different parts of the experimental set-up. This peak is thought to correspond to a low harmonic order of the ceramic tube which behaves like a resonator; for such an open tube, $f_1 = c/2L_{tube} \sim 1.2$ kHz where $L_{tube} \sim 15$ cm is the tube length and $c \sim 350$ m/s is the speed of sound for N_2 at room temperature. Owing to the very low sensitivity of the acoustic sensor for $f < 2$ kHz, we assume that the natural frequency cannot be detected so that the first peak observed in the acoustic spectra corresponds to the second harmonic ($n = 2$), *i.e.* $f_2 = nf_1 \sim 2.4$ kHz. A refined estimate taking into account the finite length of the tube by considering its length L_{tube} to diameter ∅ ratio does not affect significantly the values above, $f_1' = c/2[L_{tube} + 0.8\varnothing] \sim 1.13$ kHz so that $f_2' = nf_1' \sim 2.2$ kHz. The peak at about 2-3 kHz can also be identified as the first harmonic ($n = 1$) corresponding to the vibration mode of N_2 in the first half of the ceramic tube (enameled part *i.e.* region between the gas entrance and the permeable region with length $L_m \sim 1$ cm); with a length $L = (L_{tube} - L_m)/2 \sim 7$ cm, we obtain $f_1 = 2.5$ kHz. Peaks observed at higher frequencies are believed to be higher harmonics

corresponding to the main vibration mode of the ceramic tube. In particular, while the acoustic spectrum around [10-15 kHz] displays many intense acoustic peaks, they are likely to correspond to higher harmonics that have large amplitude because of the improved sensor sensitivity in this frequency window. For each acoustic harmonic $f < 20$ kHz, there seems to be a matching contribution in the optical measurements applied to the different pieces of the permeation cell. However, few peaks with $f > 20$ kHz in the acoustic spectrum are not observed in the laser vibrometry experiments. This result suggests that these peaks are either artefacts of the acoustic experimental method or correspond to harmonics which are not observed in the optical technique because of poor resolution/sensitivity in this frequency range. Considering that these peaks are located at about twice the frequency of the peaks observed in the acoustic spectrum [10-15 kHz], it is believed that they are not artefacts but rather correspond to physical harmonics.

3. 3. Coupling between fluid dynamic and acoustic modes

The results above provide evidence that the membrane top-layers are acoustically active when subjected to gas transport induced by an applied transmembrane pressure. To gain insight into the effect of gas permeation on acoustic emission in porous membranes, we show in **Figure 7** the minimum pressure gradient ∇P_c required for observing CAE as a function of the top-layer pore size D. ∇P_c was estimated as follows from A_{lf} as a function of ∇P when plotted in a log scale (Inserts **Figures 5b** and **5c**). Considering that $A_{lf} \sim \ln \nabla P$ when CAE is observed, we estimated ∇P_c as the intercept of $A_{lf} \sim \ln \nabla P$ with the x axis, *i.e.* $\ln \nabla P/\nabla P_c = 0$. Error bars were estimated by considering the maximum pressure where no CAE is observed and minimum pressure at which CAE is observed (other estimates for ∇P_c such as from the slopes of the curves in **Figures 5b** and **5c** below and above CAE lead to similar results which are included in the reported error bars). **Figure 7** shows that there is a clear dependence $\nabla P_c \sim 1/D$ that remains valid over about 4 orders of magnitude. Such a simple scaling can be

rationalized as explained below by invoking a minimum stress condition $\sigma > \sigma_c$. Based on the results obtained above, such a minimum stress condition relies on the coupling between the fluid hydrodynamic mode in the top-layer and the ceramic support acoustic mode. While the hydrodynamic mode corresponds to the viscous flow contribution to gas permeation, the acoustic mode is triggered by the viscous force acting on the pore surface of the top-layer (which induces a mechanical deformation provided the stress is large enough $\sigma > \sigma_C$).

Upon gas permeation, the gas flow can be assumed to be laminar as Reynolds numbers Re << 1 for all membranes taken at their threshold pressure for CAE. Moreover, as discussed above, when considering the origin of acoustic emission, the contributing gas flow through the membranes can be assumed to be purely viscous as Knudsen diffusion does not seem to generate CAE. To develop a model for CAE induced by gas flow through porous membranes, one has therefore to consider the laminar flow of a compressible gas inside the membrane top-layer porosity. However, despite the significant compressibility of N_2, CO_2 and He at room temperature, gas flow through the studied membranes can be considered as incompressible owing to the relatively low velocities induced by the pressure gradients. Indeed, for the studied membranes taken at their corresponding threshold pressure for CAE, Mach numbers, *i.e.* the ratio of the flow velocity v and sound velocity c, are $Ma = v/c < 10^{-3}$ (since the flow is assumed to be viscous, the flow velocity was estimated using Darcy's equation). Within the assumptions above, by solving Navier-Stokes equation in the laminar regime, neglecting gravity, and taking the stationary solution $\frac{\partial v}{\partial t} = 0$, we obtain the well-known Poiseuille flow where the velocity in the z direction is parabolic $v_z(r) \sim \gamma[1 - (2r/D)^2]$ where r is the radial position, D the pore diameter, and $\gamma = D^2\nabla P/16\eta$ (estimating the average velocity from the above expression is consistent with Darcy's flow where the permeability $k = D^2/32$).

Using the parabolic velocity profile, the shear stress $\sigma_{rz}(r') = -\eta \left.\frac{dv_z(r)}{dr}\right|_{r=r'}$ induced by the gas flow at a given radial position *r'* is found to be maximum at the pore surface with a value $\sigma^s = D\nabla P/4$. This stress exerted by the fluid on the pore wall can be estimated directly by considering that the viscous force $F_v = \pi DL\sigma^s$ that applies at the pore surface compensates the net pressure force inducing gas permeation $F_p = \pi D^2 \Delta P/4$ (with $\Delta P = L\nabla P$ where L is the pore length). The surface stress σ^s induces a strain ε^s in the top-layer, *i.e.* $\sigma^s = K\varepsilon^s$ with K the elastic bulk modulus, which in turn induces CAE. While in this model CAE should be observed for all strains/stresses (*i.e.* whatever their amplitude), our data suggest that σ^s has to be larger than a critical value σ_c to induce CAE. This implies that CAE is observed for $\sigma^s = D\nabla P/4 > \sigma_c$ which can be recast as $\nabla P > \nabla P_c$ with $\nabla P_c = 4\sigma_c/D$; such a scaling $\nabla P_c \sim 1/D$ is fully consistent with the results in **Figure 7**. Based on the data for N_2 at room temperature in **Figure 7**, we find $\sigma_c \sim 10^2$ Pa. To validate our model, we compare in the insert of **Figure 7** the critical pressure gradients obtained for N_2, He, and CO_2 – the data corresponding to the acoustic spectra at different pressures for He and CO_2 gases are shown in Supplementary **Figures S2** and **S3**. Although ∇P_c(He) tends to be slightly larger than for N_2 and CO_2, we find ∇P_c(He) ~ ∇P_c (CO_2) ~ ∇P_c (N_2), in agreement with our model prediction $\nabla P_c \sim 4\sigma_c/D$. Interestingly, the slight difference between He and the two other gases can be attributed to the purely non-adsorbing nature for the former; in particular, with such a non-adsorbing gas, one can expect slippage effects [34,39] (non-sticky boundary condition at the pore surface) so that larger flow velocities are required to induce sufficient surface stresses and promote acoustic emission.

4. Conclusion

Our experimental and theoretical results demonstrate that acoustic emission can be envisaged as a powerful, multiscale and non-invasive technique to investigate porous membranes subjected to external *stimuli* such as gas permeation. By establishing the intimate relationship between the acoustic footprints of *operando* porous membranes, their top-layer pore size and applied gas pressure gradient, the present study shows that gas transport can be assessed by monitoring continuous acoustic emission. In particular, the fact that acoustic emission is induced by the pressure-dependent contribution to the total gas flow (since the Knudsen contribution does not seem to induce any acoustic emission), with a minimum pressure gradient condition at the pore surface, is important for both fundamental and applied sciences. While such promising results have been obtained for stationary conditions, we believe that they remain relevant under non-stationary conditions such as upon thermal and pressure cycling but also to detect and follow the formation and evolution of cracks, defects, etc. Eventually, such proposed technique and model should allow the development of a novel *on-line*, non-destructive characterization method.

The agreement between the experimental data and the predictions of our model supports the proposed picture of continuous acoustic emission being triggered when the viscous stress reaches a critical value (so that the minimum pressure gradient required to induce acoustic emission scales with the reciprocal of the top-layer pore size). While the minimum pressure gradient in this model does not depend on the gas type in agreement with our experimental data, both the frequency and amplitude of the stimulated acoustic modes depend on the gas molecule being transported (due to their large attenuation coefficients, heavier molecules such as CO_2 yield weaker acoustic signals than lighter molecules such as He and N_2).

Extension of the present work is currently considered for gas mixtures including steams and other membrane materials (e.g. porous carbons and polymers, non-oxides or hybrid

organic/inorganic membranes). Moreover, considering that real systems under development for industrial separations possess multiscale pore structures, it is crucial to determine the acoustic response which might correspond to a complex coupling of all pore families' contributions. Such complex framework investigations will be the subject of future work.

Acknowledgements

This study, initially supported by the European Commission (CARENA project FP7-NMP-2010-LARGE) and the LabEx CheMISyst ANR-1 0-LABX-05-01 (COM-EA project – TZ/DN 12-29), received additional financial support from the Institut Carnot Chimie Balard and the Institut d'Electronique et des Systèmes at the University of Montpellier (CarOMA project AAP 2016 Carnot-IES). We are grateful to Dr. Elise Lorenceau (LIPhy, Grenoble) for very stimulating discussions.

References

[1] A. Ayral, A. Julbe, Ceramic membranes for gas treatment and Separation, in: N. Kanellopoulos (Ed.), Nanoporous Materials for Energy and the Environment, Stanford Publishing Pte. Ltd, Singapore, 2012; pp. 203–229.

[2] S. Madaeni, N. Ghaemi, H. Rajabi, Advances in Membrane Technologies for Water Treatment, in: A. Basile, A. Cassano, N.K. Rastogi, (Eds.), Materials, Processes and Applications, Woodhead Publishing, Oxford, 2015, pp. 3–41.

[3] A. Gugliuzza, A. Basile, Membranes for Clean and Renewable Power Applications; Woodhead Publishing: Oxford, 2013.

[4] F. Lipnizki, A. Dupuy, Food industry applications, in: E.M.V. Hoek, V.V. Tarabara (Eds.), Encyclopedia of Membrane Science and Technology, John Wiley and Sons, Hoboken, NJ, 2013, pp. 2102–2124.

[5] A. Brunetti, G. Barbieri, E. Drioli, Gas Separation, Applications, in: E.M.V. Hoek, V.V. Tarabara, (Eds.), Encyclopedia of Membrane Science and Technology, John Wiley and Sons, Hoboken, NJ, 2013, pp 1886–1915.

[6] D.S. Sholl, R.P Lively, Seven chemical separations to change the world. Nature 532 (2016) 435–437.

[7] M.Y. Jeon, D. Kim, P. Kumar, P.S. Lee, N. Rangnekar, P. Bai, M. Shete, B. Elyassi, H.S. Lee, K. Narasimharao, S.N. Basahel, S. Al-Thabaiti, W. Xu, H.J. Cho, E.O. Fetisov, R. Thyagarajan, R.F. DeJaco, W. Fan, K.A. Mkhoyan, J.I. Siepmann, M. Tsapatsis,. Ultra-selective high-flux membranes from directly synthesized zeolite nanosheets, Nature 543 (2017) 690–694.

[8] R. Dittmeyer, J. Caro, Catalytic Membrane Reactors, in: G. Ertl, H. Knözinger, F. Schüth, J. Weitkamp (Eds.), Handbook of Heterogeneous Catalysis, John Wiley and Sons, Weinheim, 2008, pp. 2198–2248.

[9] L.M. Gandia, G. Arzamendi, P.M. Diéguez, Renewable hydrogen technologies: production, purification, storage, applications and safety, Elsevier, Netherlands, 2013.

[10] J. Choi, H.K. Jeong, M.A. Snyder, J.A. Stoeger, R.I. Masel, M. Tsapatsis, Grain boundary defect elimination in a zeolite membrane by rapid thermal processing, Science 325 (2009) 590–593.

[11] K. Varoon, X. Zhang, B. Elyassi, D.D. Brewer, M. Gettel, S. Kumar, J.A. Lee, S. Maheshwari, A. Mittal, C.Y. Sung, M. Cococcioni, L.F. Francis, A.V. Mc Cormick, K.A. Mkhoyan, M. Tsapatsis, Dispersible exfoliated zeolite nanosheets and their application as a selective membrane, Science 334 (2011) 72–75.

[12] M. Mulder, Characterization of membranes, in: M. Mulder (Ed.), Basic Principles of Membrane Technology, Kluwer Academic Publishers, Netherlands 1991, pp 110-133.

[13] H.P. Hsieh, General Characteristics of Inorganic Membranes, in: R.R. Bhave, (Ed.) Inorganic Membranes, Synthesis, Characteristics and Applications, Van Nostrand Reinhold: New York, 1991, pp 64–94.

[14] A. Julbe, J.D. F Ramsay, Methods for the characterisation of porous structure in membrane materials, in: A.J. Burggraaf, L. Cot, (Eds.), Fundamentals of Inorganic Membrane Science and Technology, Membrane Sci. and Technol. Series 4, Elsevier, Amsterdam 1996, pp 67–118.

[15] Y. Cai, J. Li, Y. Guo, Z. Cui, Y. Zhang, In-situ monitoring of asymmetric poly(ethylene-co-vinyl alcohol) membrane formation via a phase inversion process by ultrasonic through-transmission technique, Desalination 283 (2011) 25–30.

[16] Y.L. Hou, Y. Gao, Y. Cai, X. Xu, J. Li, In-situ monitoring of inorganic and microbial synergistic fouling during nanofiltration by UTDR. Desal. Wat. Treat. 11 (2009) 15–22.

[17] J-X. Li, R.D. Sanderson, G.Y. Chai, A focused ultrasonic sensor for in-situ detection of protein fouling on tubular ultrafiltration membranes, Sens. Actuator B-Chem. B 114 (2006) 182–192.

[18] Z. Zhang, V.M. Bright, A.R. Greenberg, Use of capacitive microsensors and ultrasonic time-domain reflectometry for in-situ quantification of concentration polarization and membrane fouling in pressure-driven membrane filtration. Sens. Actuator B-Chem. B 117 (2006) 323–331.

[19] J. Kim, P.K. Liaw, The Nondestructive Evaluation of Advanced Ceramics and Ceramic-Matrix Composites. J. Mater. 50 (1998) 1–15.

[20] Standard Terminology for Nondestructive Examinations, E1316-96 (Philadelphia, PA: ASTM, 1996).

[21] T.J. Chotard, A. Smith, D. Rotureau, D. Fargeot, C. Gault, Acoustic emission characterisation of calcium aluminate cement hydration at an early stage, J. Eur. Cer. Soc. 23 (2003) 387–398.

[22] S.J. Kowalski, Control of mechanical processes in drying. Theory and experiment. Chem. Eng. Sci. 65 (2010) 890–899.

[23] J.R. Lee, H. Tsuda, A novel fiber Bragg grating acoustic emission sensor head for mechanical tests, Scripta Materialia 53 (2005) 1181–1186.

[24] B. Legros, P.-X. Thivel, Y. Bultel, M. Boinet, R.P. Nogueira, Acoustic emission: Towards a real-time diagnosis technique for Proton Exchange Membrane Fuel Cell operation, J. Power. Sources 195 (2010) 8124–8133.

[25] G. Michlmayr, D. Cohen, D. Or. Sources and characteristics of acoustic emissions from mechanically stressed geologic granular media - a review. Earth-Science Reviews, 112 (2012) 97–114.

[26] G. Michlmayr, D. Cohen, D. Or. Shear-induced force fluctuations and acoustic emissions in granular material. J. Geophys. Res. –Sol. Ea. 118 (2013) 6086–6098.

[27] E. D. Manga, H. Blasco, P. Da-Costa, M. Drobek, A. Ayral, E. Le Clezio, G. Despaux, B. Coasne and A. Julbe. Effect of Gas Adsorption on Acoustic Wave Propagation in MFI Zeolite Membrane Materials: Experiment and Molecular Simulation, Langmuir 30 (2014) 10336−10343.

[28] J. Rouquerol, D. Avnir, C. W. Fairbridge, D. H. Everett, J. M. Haynes, N. Pernicone, J. D. F. Ramsay, K. S. W. Sing and K. K. Unger, recommendations for the characterization of porous solids, Pure & Appl. Chem. 66 (1994)1739-1758.

[29] M. Drobek, J. Motuzas, M. Van Loon, R.W.J. Dirrix, R.A. Terpstra, A. Julbe, Coupling microwave-assisted and classical heating methods for scaling-up MFI zeolite membrane synthesis, J. Membr. Sci. 401-402 (2012) 144–151.

[30] N.N. Hsu, F.R. Breckenridge, Characterization and calibration of acoustic emission sensors, Mater. Eval. 39, (1981) 60–68.

[31] R.M. Fand, B.Y.K. Kim, A.C.C. Lam, R.T. Phan, Resistance to the flow of fluids through simple and complex porous media whose matrices are composed of randomly packed spheres, Journal of Fluids Engineering 109 (1987) 268–273.

[32] A.J. Burggraaf, Transport and separation properties of membranes with gases and vapours, in: A.J. Burggraaf, L. Cot, (Eds.), Fundamentals of Inorganic Membrane Science and Technology, Membrane Sci. and Technol. Series 4 – Elsevier, Amsterdam, 1996, pp. 331–433.

[33] B. Coasne, Multiscale adsorption and transport in hierarchical porous materials, New Journal of Chemistry 40 (2016) 4078–4094.

[34] L. Bocquet, E. Charlaix, Nanofluidics, from bulk to interfaces, Chemical Society Reviews 39 (2010) 1073–1095.

[35] K. Falk, B. Coasne, R. Pellenq, F-Z Ulm and L. Bocquet. Subcontinuum mass transport of condensed hydrocarbons in nanoporous media. Nature Comm. 6 (2015) 6949-1–6949-7

[36] A. Obliger, R. Pellenq, F-Z. Ulm and B. Coasne. Free volume theory of hydrocarbon mixture transport in nanoporous materials. J. Phys. Chem. Lett. 7 (2016) 3712–3717.

[37] T. Delaunay, E. Le Clézio, M. Guennou, H. Dammak, , M. Pham-Thi, G. Feuillard, Full tensorial characterization of PZN-12%PT single crystal by resonant ultrasound spectroscopy, IEEE Transactions on Ultrasonics, Ferroelectrics, and Frequency Control 55 (2008) 476–488.

[38] R. Longo, T. Delaunay, D. Laux, M. El Mouridi, O. Arnould, E. Le Clézio, Wood elastic characterization from a single sample by resonant ultrasound spectroscopy, Ultrasonics 52 (2012) 971–974.

[39] C. Cottin-Bizonne, J.-L. Barrat, L. Bocquet, E. Charlaix, Low-friction flows of liquid at nanopatterned interfaces, Nature Materials 2 (2003) 237–240.

Figure captions:

Figure 1: Schematic representation of the morphology and asymmetric microstructure of the studied porous ceramic membranes.

Figure 2: Schematic representation of the experimental set-up for continuous acoustic emission (CAE) measurements during single gas permeation tests.

Figure 3: N_2 single gas permeances (with linear fits) as function of mean pressure ($P_m = 0.5\Delta P + P_{atm}$) through the porous membranes with top-layer pore sizes: D ~ 0.55 nm (green), D ~ 8 nm (blue), D ~ 55 nm (black), D ~ 100 nm (purple), and D ~ 800 nm (red). Insert: permeance of N_2 (circles), CO_2 (triangles), and He (squares) through the membrane with top-layer pore size D ~ 55 nm. (permeance and pressure units are the same as in the main figure).

Figure 4: CAE amplitude as a function of frequency f and time t upon N_2 permeation through porous membranes with top-layer pore sizes: D ~ 10 μm, D ~ 800 nm, D ~ 100 nm, D ~ 55 nm, D ~ 8 nm, and D ~ 0.55 nm. (CAE amplitude increases according to the following color code: violet (no noticeable acoustic event), blue, green, and white).

Figure 5: Pressure dependence of CAE in porous membranes: **a)** Acoustic spectra of the membrane with $D \sim 10$ μm for the different transmembrane pressures $\Delta P = 0$, 1, 2, 3, 4, and 5 bar (for the sake of clarity, the data for $\Delta P = 1$, 2, 3, 4, and 5 bar are shifted up by +10, +20, +30, +40, and +50 along the y axis, respectively), b) CAE amplitude A_{lf} as a function of transmembrane pressure upon N_2 permeation through porous membranes with top-layer pore sizes $D \sim 0.55$ nm (green), $D \sim 8$ nm (blue), $D \sim 55$ nm (black), $D \sim 100$ nm (purple), $D \sim 800$ nm (red), and $D \sim 10$ μm (light blue) at the resonance frequency $f \sim 10$ kHz (insert shows the same data with frequencies (x-axis) in a log scale), **c)** Same as **b)** but for the acoustic amplitude $\tilde{A}_{hf}$ integrated at high frequency over the range [146-190 kHz].

Figure 6: Acoustic and optical measurements for acoustic mode identification: **a)** Acoustic spectrum in the frequency range [0-40 kHz] for the membrane with top-layer pore size $D \sim 100$ nm at $\Delta P = 4$ bar (amplitude on y-axis is shown in a log scale to highlight the different acoustic peaks). The colored vertical arrows correspond to the modes identified using optical measurements in (b) where the different components of the set-up are considered. The shaded pink area corresponds to peaks in the frequency range [~20-26 kHz] and is assumed to correspond to higher harmonic modes of those observed in the frequency range [10-15 kHz]. **(b)** Vibration modes for the membrane with top-layer pore size $D \sim 100$ nm at $\Delta P = 4$ bar as probed using laser vibrometry. With such measurements, the different set-up components in **Figure 2** are analyzed: gas entrance from the source/gas feed, gas exit towards the flowmeter, Al disc attached to the ceramic membrane, and ceramic support itself on which other layers are deposited. The vertical arrows indicate some of the main modes probed using this optical technique that are identified in the acoustic measurements in **(a).**

Figure 7: Pressure gradient threshold for continuous acoustic emission in porous membranes, ∇P_c - minimum pressure gradient to observe CAE upon N_2 gas permeation as a

function of top-layer pore size D. The dashed blue line shows a power law scaling $\nabla P_c \sim 1/D$. ∇P_c is determined from the pressure above which the acoustic amplitude A_{lf} at the frequency $f \sim 10$ kHz becomes different from zero. The plot is obtained from the data shown in Fig. 4 for top-layer pores sizes: $D \sim 8$ nm, 55 nm, 100 nm, $D \sim 800$ nm, and 10 μm (no CAE was observed for the top-layer pore size $D \sim 0.5$ nm with the pressure gradients tested here). The insert shows the minimum pressure gradient ∇P_c observed for CO_2 (blue triangles) and He (red squares) as a function of ∇P_c observed for N_2. The black dashed line indicates the bissector $\nabla P_c(CO_2) = \nabla P_c(N_2)$ or $\nabla P_c(He) = \nabla P_c(N_2)$.

Supplementary Figure captions:

Supplementary Figure S1: Frequency-time spectrum recorded during N_2 permeation through the membrane with top-layer pore size $D \sim 800$ nm. Region A corresponds to the high frequency range within the sensor operating range. Region B corresponds to the low frequency range out of the sensor bandwidth i.e. 50 – 400 kHz for the thickness mode & within the sensor bandwidth (data not provided by the supplier) for the radial mode.

Supplementary Figure S2: Continuous acoustic emission spectra recorded during gas permeation through the membrane with top-layer pore size $D \sim 55$ nm. The CAE amplitude was recorded as a function of frequency f and time t during N_2 (*left side*), CO_2 (*middle*) and He (*right*) permeation. The CAE amplitude increases according to the following color code: violet (no noticeable acoustic event), blue, green, and white.

Supplementary Figure S3 | Pressure gradient dependence of CAE induced by different gases. CAE amplitude as a function of transmembrane pressure during N_2 (circles), CO_2 (triangles), and He (squares) permeation through membranes with different top-layer pore sizes. Acoustic amplitude A_{lf} at the natural resonance frequency of the ceramic tube ($f \sim 10$ kHz) are plotted for membranes with top-layer pore sizes: $D \sim 55$ nm (black), $D \sim 100$ nm (purple), and $D \sim 800$ nm (red).

Table captions:

Table 1: Characteristics of the tubular ceramic membranes investigated in this work.

Table 2: Main physical properties of the single gases used in permeation measurements

Supplementary Table captions:

Supplementary Table S1: Slopes (a) and intercepts (b) corresponding to linear fits of the permeance $\Pi = aP_m + b$ for porous membranes with different top-layer pore size D & viscous flow contribution, aP_m, in % to the total flow for $\Delta P = 0.5$ bar.

Supplementary Table S2: Slopes (a) and intercepts (b) corresponding to linear fits of the permeance $\Pi = aP_m + b$ for He, N_2 and CO_2 for membrane with a $D = 55$ nm top-layer a pore size (the number in parentheses is the error bar) & viscous flow contribution, aP_m, in % to the total flow for $\Delta P = 0.5$ bar.

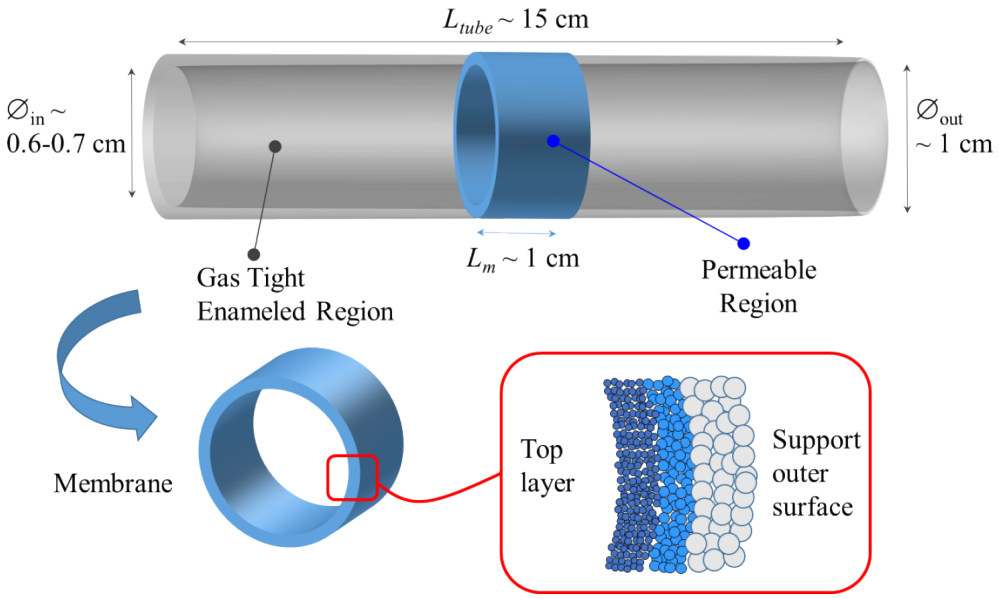

Figure 1 | Schematic representation of the morphology and asymmetric microstructure of the studied porous ceramic membranes.

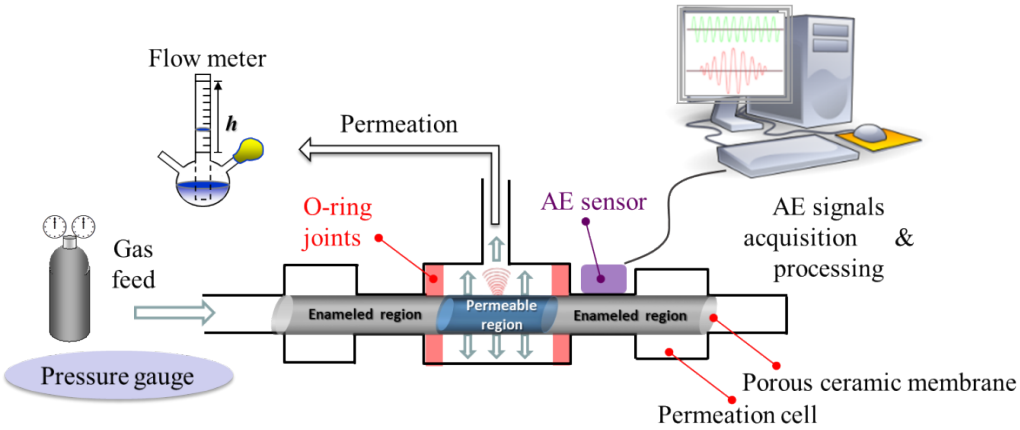

Figure 2. Schematic representation of the experimental set-up for continuous acoustic emission (CAE) measurements during single gas permeation tests.

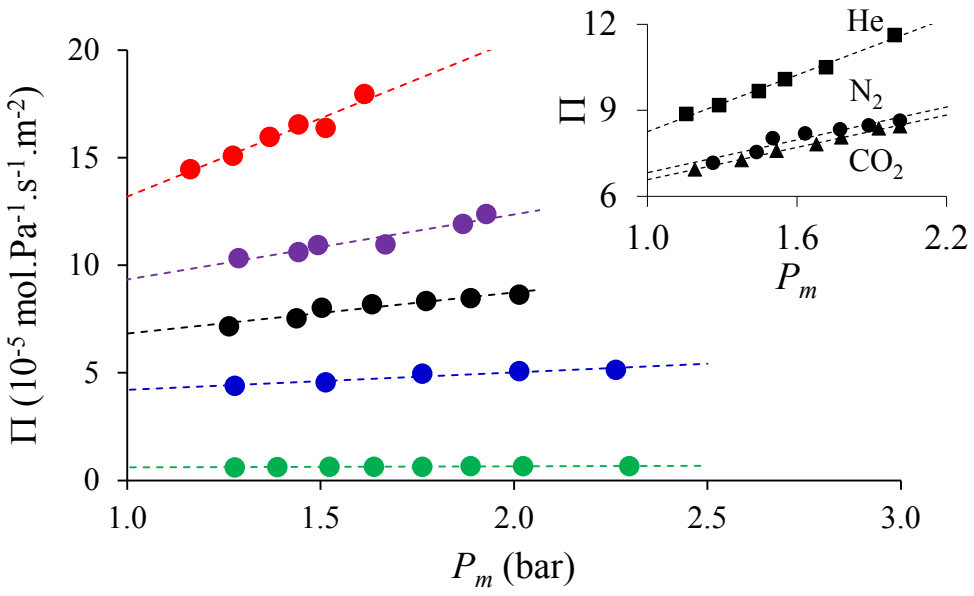

Figure 3 | N_2 single gas permeances (with linear fits) as function of mean pressure ($P_m = 0.5\Delta P + P_{atm}$) through the porous membranes with top-layer pore sizes: $D \sim 0.55$ nm (green), $D \sim 8$ nm (blue), $D \sim 55$ nm (black), $D \sim 100$ nm (purple), and $D \sim 800$ nm (red).
Insert: permeance of N_2 (circles), CO_2 (triangles), and He (squares) through the membrane with top-layer pore size $D \sim 55$ nm. (permeance and pressure units are the same as in the main figure).

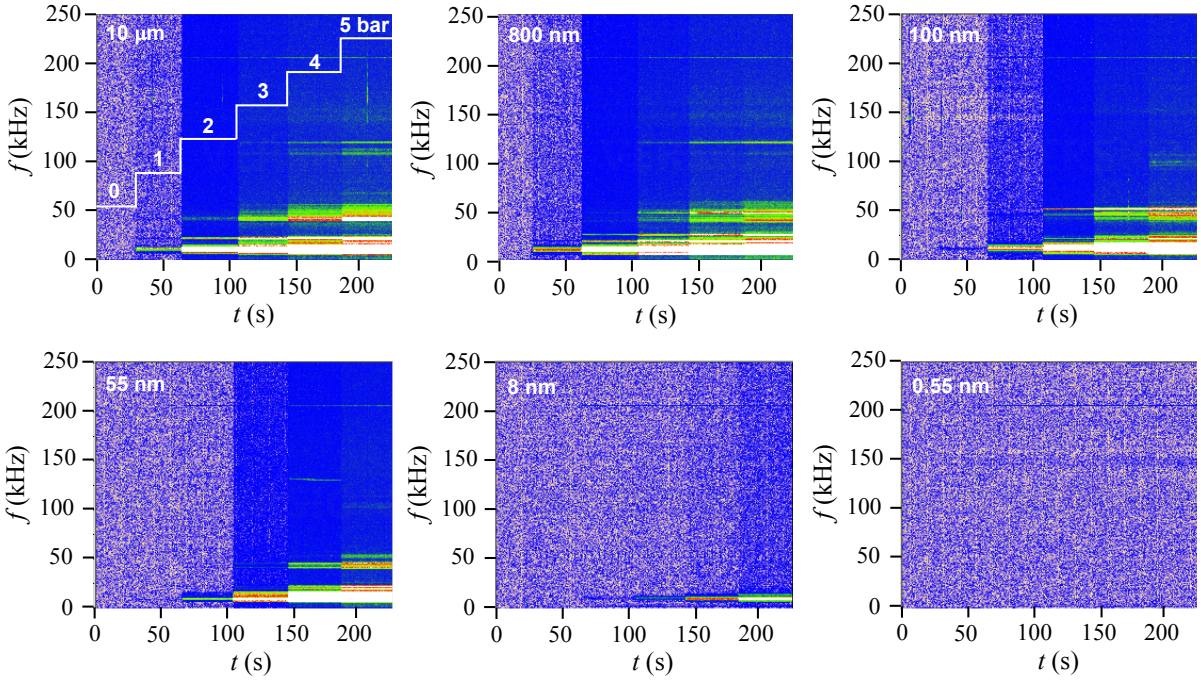

Figure 4 | CAE amplitude as a function of frequency f and time t upon N_2 permeation through porous membranes with top-layer pore sizes: $D \sim 10$ µm, $D \sim 800$ nm, $D \sim 100$ nm, $D \sim 55$ nm, $D \sim 8$ nm, and $D \sim 0.55$ nm. (CAE amplitude increases according to the following color code: violet (no noticeable acoustic event), blue, green, and white).

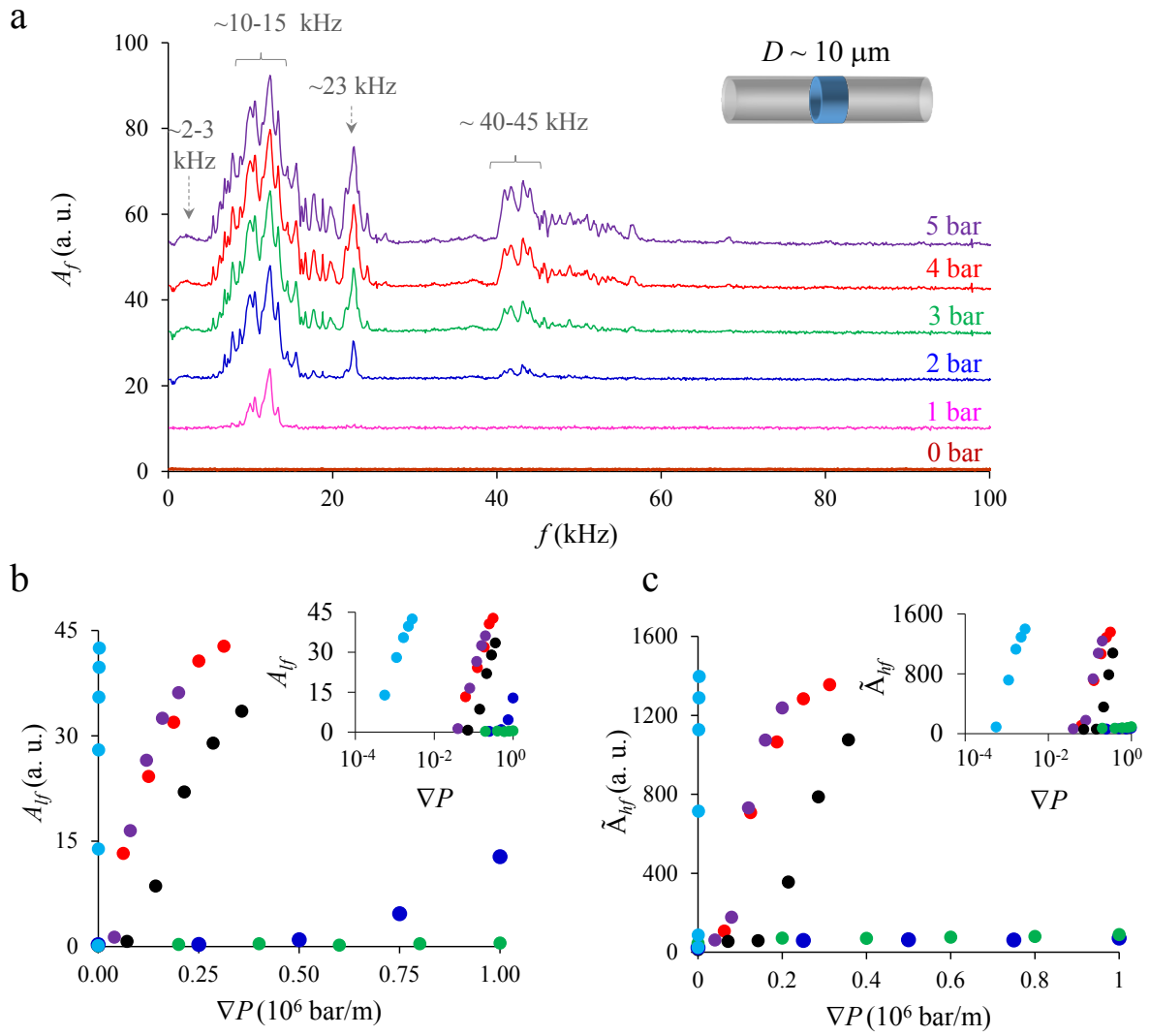

Figure 5 | Pressure dependence of CAE in porous membranes: **a)** Acoustic spectra of the membrane with $D \sim 10$ µm for the different transmembrane pressures $\Delta P = 0$, 1, 2, 3, 4, and 5 bar (for the sake of clarity, the data for $\Delta P = 1$, 2, 3, 4, and 5 bar are shifted up by +10, +20, +30, +40, and +50 along the y axis, respectively), **b)** CAE amplitude A_{lf} as a function of transmembrane pressure upon N_2 permeation through porous membranes with top-layer pore sizes $D \sim 0.55$ nm (green), $D \sim 8$ nm (blue), $D \sim 55$ nm (black), $D \sim 100$ nm (purple), $D \sim 800$ nm (red), and $D \sim 10$ µm (light blue) at the resonance frequency $f \sim 10$ kHz (insert shows the same data with frequencies (x-axis) in a log scale), **c)** Same as **b)** but for the acoustic amplitude $\tilde{A}_{hf}$ integrated at high frequency over the range [146-190 kHz].

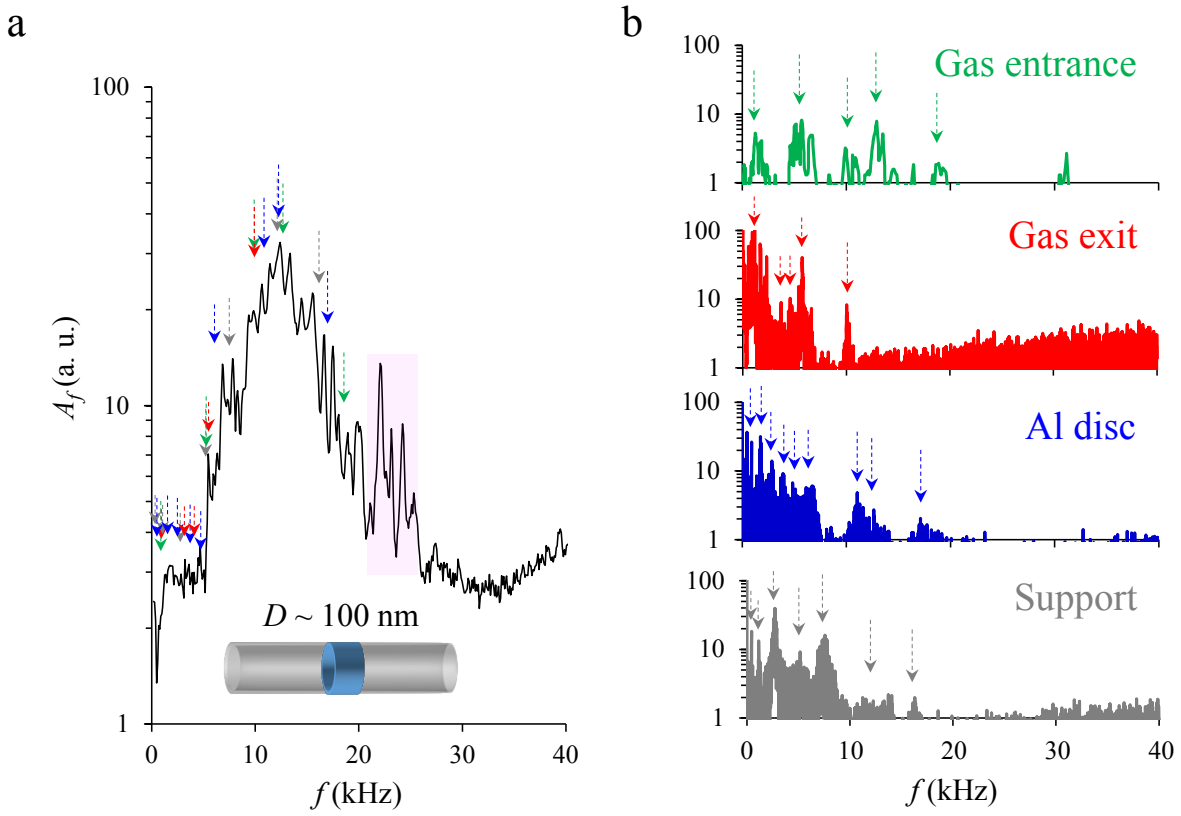

Figure 6 | Acoustic and optical measurements for acoustic mode identification: **a)** Acoustic spectrum in the frequency range [0-40 kHz] for the membrane with top-layer pore size D ~ 100 nm at ΔP = 4 bar (amplitude on y-axis is shown in a log scale to highlight the different acoustic peaks). The colored vertical arrows correspond to the modes identified using optical measurements in (b) where the different components of the set-up are considered. The shaded pink area corresponds to peaks in the frequency range [~20-26 kHz] and is assumed to correspond to higher harmonic modes of those observed in the frequency range [10-15 kHz]. **(b)** Vibration modes for the membrane with top-layer pore size D ~ 100 nm at ΔP = 4 bar as probed using laser vibrometry. With such measurements, the different set-up components in **Figure 2** are analyzed: gas entrance from the source/gas feed, gas exit towards the flowmeter, Al disc attached to the ceramic membrane, and ceramic support itself on which other layers are deposited. The vertical arrows indicate some of the main modes probed using this optical technique that are identified in the acoustic measurements in **(a).**

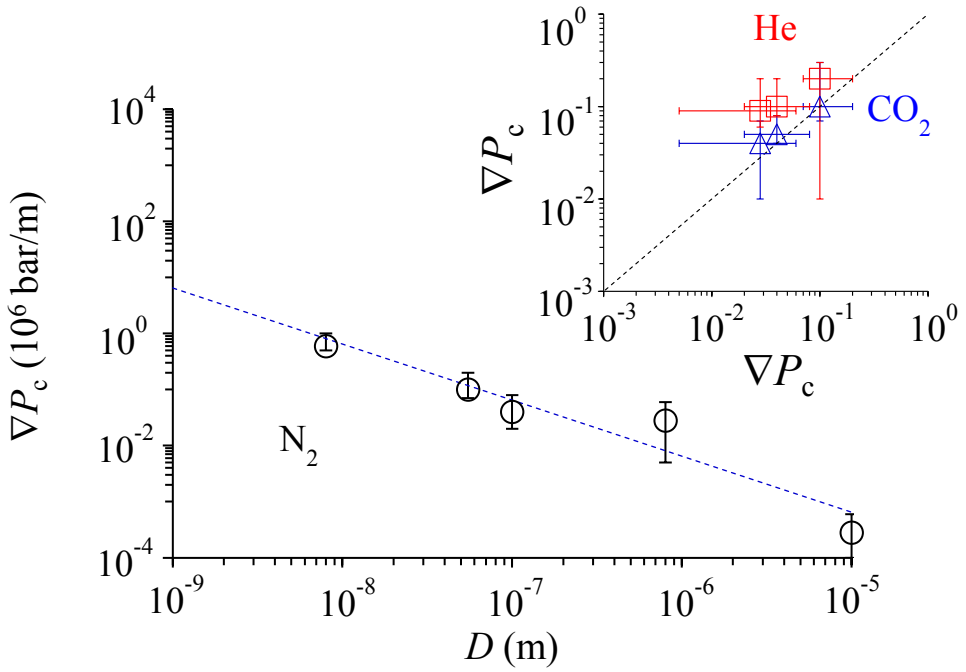

Figure 7 | Pressure gradient threshold for continuous acoustic emission in porous membranes, ∇P_c - minimum pressure gradient to observe CAE upon N_2 gas permeation as a function of top-layer pore size D. The dashed blue line shows a power law scaling $\nabla P_c \sim 1/D$. ∇P_c is determined from the pressure above which the acoustic amplitude A_{lf} at the frequency $f \sim 10$ kHz becomes different from zero. The plot is obtained from the data shown in Fig. 4 for top-layer pores sizes: $D \sim 8$ nm, 55 nm, 100 nm, $D \sim 800$ nm, and 10 μm (no CAE was observed for the top-layer pore size $D \sim 0.5$ nm with the pressure gradients tested here). The insert shows the minimum pressure gradient ∇P_c observed for CO_2 (blue triangles) and He (red squares) as a function of ∇P_c observed for N_2. The black dashed line indicates the bissector $\nabla P_c(CO_2) = \nabla P_c(N_2)$ or $\nabla P_c(He) = \nabla P_c(N_2)$.

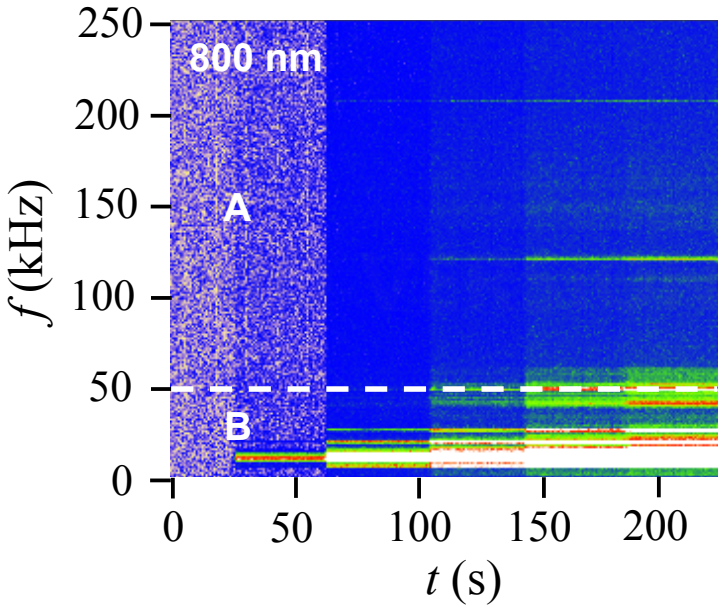

Supplementary Figure S1 | Frequency-time spectrum recorded during N_2 permeation through the membrane with top-layer pore size D ~ 800 nm. Region A corresponds to the high frequency range within the sensor operating range. Region B corresponds to the low frequency range out of the sensor bandwidth i.e. 50 – 400 kHz for the thickness mode & within the sensor bandwidth (data not provided by the supplier) for the radial mode.

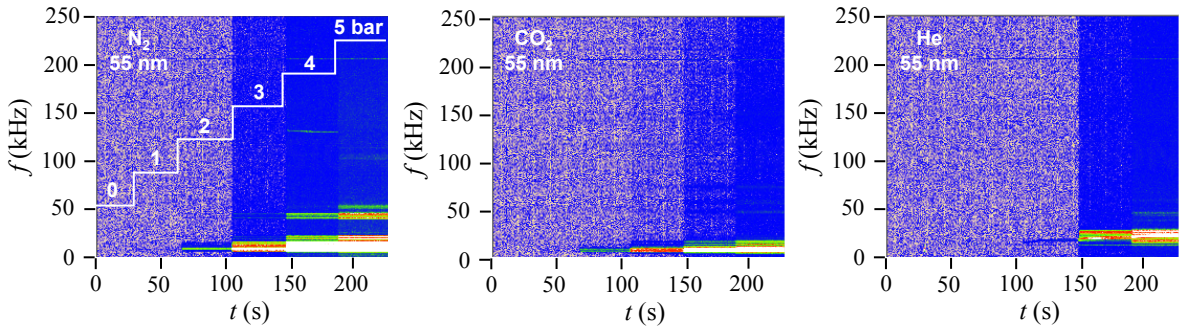

Supplementary Figure S2 | Continuous acoustic emission spectra recorded during gas permeation through the membrane with top-layer pore size $D \sim 55$ nm. The CAE amplitude was recorded as a function of frequency f and time t during N_2 (*left side*), CO_2 (*middle*) and He (*right*) permeation. The CAE amplitude increases according to the following color code: violet (no noticeable acoustic event), blue, green, and white.

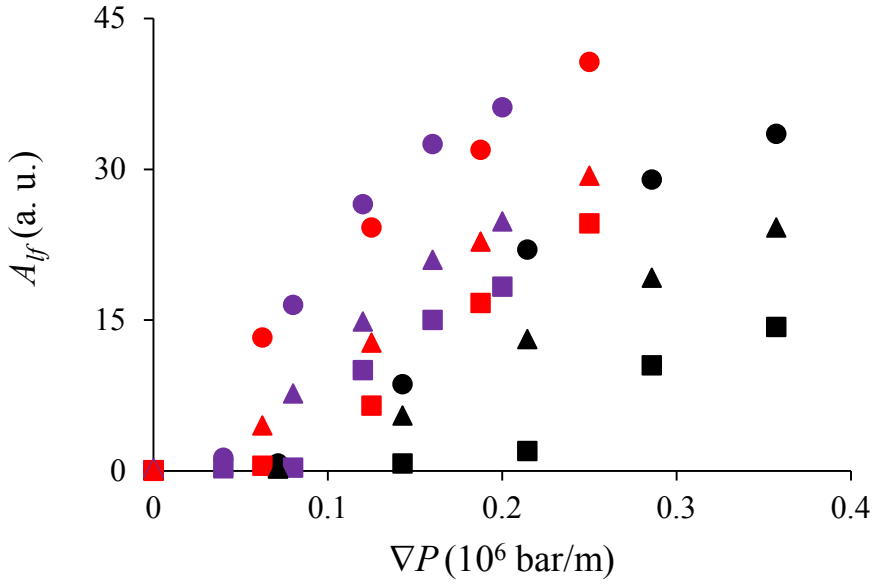

Supplementary Figure S3 | Pressure gradient dependence of CAE induced by different gases. CAE amplitude as a function of transmembrane pressure during N_2 (circles), CO_2 (triangles), and He (squares) permeation through membranes with different top-layer pore sizes. Acoustic amplitude A_{lf} at the natural resonance frequency of the ceramic tube ($f \sim 10$ kHz) are plotted for membranes with top-layer pore sizes: $D \sim 55$ nm (black), $D \sim 100$ nm (purple), and $D \sim 800$ nm (red).

Table 1 | Characteristics of the tubular ceramic membranes investigated in this work.

Membrane ref.	Provider	Top-layer material	Top-layer support	Tube length L_{tube} (mm)	Tube diameters		Length of permeable region L_m (mm)	Mean pore diameter D (nm)	Surface of permeable region S (mm^2)	Top-layer thickness t (µm)
					$\varnothing_{in}$ (mm)	$\varnothing_{out}$ (mm)				
0.55 nm	IEM[#]	MFI	Pall-Exekia α-Al_2O_3 200 nm (3 layers)	150	7	10	15.0	0.55	330	5
8 nm	Pall-Exekia	γ-Al_2O_3	Pall-Exekia α-Al_2O_3 200 nm (3 layers)	145	7	10	9.7	5* (8)	214	4
55 nm	Atech	Al_2O_3/TiO_2	Atech α-Al_2O_3 200 nm (2 layers)	150	6	10	9.6	50* (55)	181	14
100 nm	Atech	α-Al_2O_3	Atech α-Al_2O_3 1.2 µm (1 layer)	150	6	10	8.9	100	168	25
800 nm	Pall-Exekia	α-Al_2O_3	Pall-Exekia α-Al_2O_3 10 µm (1 layer)	150	7	10	8.2	800	180	16
10 µm	CTI	α-Al_2O_3	(support by itself)	145	7	10	10.0	10000	220	1800

 # The MFI membrane was prepared according to the protocol described in [27].

****** Mean pore size before enameling (mean pore size after enameling is in brackets)***

Table 2 | Main physical properties of the single gases used in permeation measurements

Gas	Molecular weight M (g/mol)	Density ρ (kg/m^3), 25°C, 10^5 Pa	Dynamic viscosity η (10^{-5} kg/m.s), 25°C, 10^5 Pa	Mean free path λ (Å), 25°C, 10^5 Pa	Kinetic diameter $\emptyset_K$ (Å)	Lennard-Jones $\emptyset_L$ (Å)
He	4.00	0.164	1.98	2809	2.60	2.55
N_2	28.01	1.145	1.78	947	3.64	3.80
CO_2	44.01	1.810	1.49	628	3.30	3.94

Supplementary Table S1| Slopes (a) and intercepts (b) corresponding to linear fits of the permeance $\Pi = aP_m + b$ for porous membranes with different top-layer pore size D & viscous flow contribution, aP_m, in % to the total flow for $\Delta P = 0.5$ bar.

Top-layer pore size D (nm)	a (10^{-10} mol.Pa^{-2}.m^{-2}.s^{-1})	b (10^{-5} mol.Pa^{-1}.m^{-2}.s^{-1})	Viscous flow (%)
800	7.30 (0.9)	5.90 (1.3)	59
100	3.00 (0.5)	6.30 (0.8)	39
55	1.90 (0.3)	4.90 (0.5)	31
8	0.73 (0.11)	3.50 (0.2)	19
0.55	0.05 (0.01)	0.56 (0.02)	8

Supplementary Table S2| Slopes (a) and intercepts (b) corresponding to linear fits of the permeance $\Pi = aP_m + b$ for He, N_2 and CO_2 for membrane with a D = 55 nm top-layer a pore size (the number in parentheses is the error bar) & viscous flow contribution, aP_m, in % to the total flow for ΔP = 0.5 bar.

Gas	a (10^{-10} mol.Pa^{-2}.m^{-2}.s^{-1})	b (10^{-5} mol.Pa^{-1}m^{-2}.s^{-1})	Viscous flow (%)
He	3.30 (0.2)	5.90 (1.3)	46
N_2	1.90 (0.3)	4.90 (0.5)	31
CO_2	1.88 (0.06)	4.70 (0.09)	32